Giant Thermal Enhancement of the Electric Polarization in Ferrimagnetic $BiFe_{1-x}Co_xO_3$ Solid Solutions Near Room Temperature

César Menéndez[1] and Claudio Cazorla[1]

[1] *School of Materials Science and Engineering, UNSW Sydney, Sydney, NSW 2052, Australia*

Thermal excitations typically reduce the electric polarization in ferroelectric materials. Here, we show by means of first-principles calculations that multiferroic $BiFe_{1-x}Co_xO_3$ solid solutions with $0.25 \leq x \leq 0.50$ (BFCO) represent a noteworthy exception to this behaviour. In particular, we find that at room temperature and for moderate pressures of 0.1–1.0 GPa, depending on the composition, the electric polarization of bulk BFCO increases by $\sim 200\%$. The origin of such an exceptional behavior is a phase transformation involving a low-T rhombohedral ($\mathcal{R}$) phase and a high-T super-tetragonal ($\mathcal{T}$) phase. Both $\mathcal{R}$ and $\mathcal{T}$ phases are ferrimagnetic near room temperature with an approximate net magnetization of 0.13 μ_B per formula unit. Contrarily to what occurs in either bulk $BiFeO_3$ or $BiCoO_3$, the $\mathcal{T}$ phase is stabilized over the $\mathcal{R}$ by increasing temperature due to its higher vibrational entropy. This extraordinary T-induced $\mathcal{R} \rightarrow \mathcal{T}$ phase transition is originated by polar phonon modes involving concerted displacements of transition-metal and oxygen ions.

Super-tetragonal ($\mathcal{T}$) oxide perovskites comprise a family of materials that are fundamentally intriguing and have great potential for ferroelectric, piezoelectric, sensor, and energy conversion applications [1–3]. Super-tetragonal phases exhibit giant electric polarizations of the order of 100 $\mu C/cm^2$ and may be accompanied by magnetism [4–6]. The coexistence of ferroelectricity and magnetism in crystals, known as multiferroics, offers the possibility of controlling the magnetization with electric fields via their order-parameter coupling. Such a magnetoelectric coupling can be used, for example, to design ultra efficient logic and memory devices and realize large piezomagnetic coefficients for the miniaturization of antennas and sensors [7–10]. Furthermore, phase transitions involving $\mathcal{T}$ phases typically exhibit colossal volume changes of $\sim 10\%$ (e.g., $PbVO_3$ and related solid solutions), which can be exploited in mechanical degradation [11, 12] and solid-state cooling [13–15] applications. Examples of $\mathcal{T}$ multiferroic materials are bulk $BiCoO_3$ (BCO) and $BiFeO_3$ (BFO) thin films [16, 17].

Nonetheless, $\mathcal{T}$ phases usually are thermodynamically too stable and hence difficult to switch by means of an external field or temperature, which severely limits their technological applicability. For example, in order to stabilize a paraelectric phase in multiferroic $\mathcal{T}$ $BiCoO_3$ it is necessary to increase its temperature above 800 K or apply a large hydrostatic pressure of $P > 3$ GPa [18–20]. Likewise, the region in which the functionality of super-tetragonal $BiFeO_3$ thin films can be exploited corresponds to a narrow epitaxial strain interval in which the $\mathcal{T}$ phase coexists with a different polymorph and as a result becomes structurally soft [21, 22]. Moreover, $\mathcal{T}$ multiferroics mostly are antiferromagnetic (i.e., their atomic magnetic moments align antiparallel rendering negligible net magnetizations) and consequently are unresponsive to external magnetic fields [23]. Therefore, it is highly desirable to find new $\mathcal{T}$ multiferroic materials that react significantly to external bias near ambient conditions.

In this Letter, we show by means of first-principles calculations based on density functional theory (DFT) that $BiFe_{1-x}Co_xO_3$ solid solutions (BFCO) with $0.25 \leq x \leq 0.50$ represent ideal bulk systems in which to realize the full potential of multiferroic $\mathcal{T}$ phases. Specifically, we find that under moderate hydrostatic pressures of $0.1 \lesssim P \lesssim 1$ GPa (depending on the composition) it is possible to trigger a phase transition from a low-T rhombohedral ($\mathcal{R}$) phase to a high-T $\mathcal{T}$ phase at room temperature. The disclosed T-induced $\mathcal{R} \rightarrow \mathcal{T}$ phase transformation involves (i) a colossal increase in the electric polarization of $\Delta p \sim 200\%$, (ii) the existence of a robust net magnetization of ≈ 0.13 μ_B per formula unit (f.u.), and (iii) a giant volume increase of $\Delta V \sim 10\%$. Examples of technologies in which these multifunctional phenomena could have an immediate impact include pyroelectric energy harvesting (the T-induced variation of the electric polarization is tremendous [24, 25]) and solid-

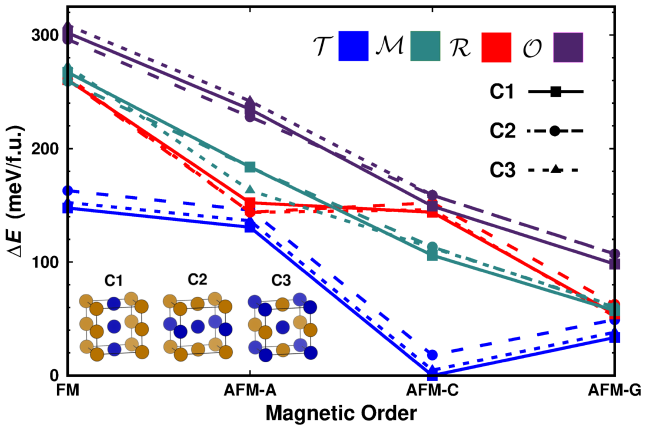

FIG. 1. First-principles analysis of bulk $BiFe_{0.5}Co_{0.5}O_3$ at zero pressure and $T = 0$. Crystal structures with tetragonal ($\mathcal{T}$), monoclinic ($\mathcal{M}$), rhombohedral ($\mathcal{R}$), and orthorhombic ($\mathcal{O}$) symmetry were considered (Supplementary Fig.1). All possible Co–Fe (C1, C2, and C3) and magnetic spin arrangements (ferromagnetic –FM– and antiferromagnetic –AFM– of type A, C, and G –Supplementary Fig.1–) were generated for a $2 \times \sqrt{2} \times \sqrt{2}$ simulation cell containing 20 atoms [34].

state cooling (multicaloric effects involving the materials response to both pressure and magnetic fields could be engineered to overcome practical limiting issues [26]). Meanwhile, the appearance of ferrimagnetism and observation that temperature stabilizes the $\mathcal{T}$ phase over the $\mathcal{R}$, effects that are missing in bulk $BiCoO_3$ and $BiFeO_3$, pose a series of interesting fundamental questions: Which atomistic mechanisms are responsible for such an anomalous $dp/dT \gg 0$ behaviour? What type of thermal excitations drive the uncovered $\mathcal{R} \rightarrow \mathcal{T}$ transformation? Why Co–Fe cation mixing triggers a net magnetization in bulk BFCO? Based on our DFT outcomes and analysis, we address these questions and make insightful connections with the experimental results reported recently for $BiFe_{1-x}Co_xO_3$ solid solutions [27–29].

Spin-polarized DFT calculations were performed with the generalized gradient approximation proposed by Perdew, Burke and Ernzerhof (PBE) as implemented in the VASP package [30, 31]. The "Hubbard-U" scheme derived by Dudarev *et al.* was employed for the description of Co (Fe) $3d$ electrons by adopting a U value of 6 (4) eV [19, 20, 32]. The "projected augmented wave" method [33] was used to represent the ionic cores by considering the following electronic states as valence: Co $4s^13d^8$, Fe $3p^64s^13d^7$, Bi $6s^25d^{10}6p^3$, and O $2s^22p^4$. An energy cut-off of 800 eV and a Γ-centered **k**-point grid of $4 \times 6 \times 6$ were employed for a $2 \times \sqrt{2} \times \sqrt{2}$ simulation cell containing 20 atoms [34], thus obtaining zero-temperature energies converged to within 0.5 meV/f.u. Geometry relaxations were performed for an atomic force threshold of 0.005 eV·Å^{-1}. Electric polarizations were estimated perturbatively by considering the atomic displacements referred to a non-polar reference phase and the corresponding Born effective charges tensor [34]. *Ab initio* free energies were calculated within the quasi-harmonic (QH) approximation [32, 35] as a function of P and T. Phonon frequencies were calculated with the small displacement method [36, 37]. The following technical parameters provided QH free energies converged to within 5 meV/f.u.: 160-atom supercells, atomic displacements of 0.01 Å, and q-point grids of $16 \times 16 \times 16$ for integration within the first Brillouin zone. The effects of chemical disorder were addressed by generating all possible atomic Co–Fe and magnetic spin arrangements (ferromagnetic –FM– and antiferromagnetic –AFM– of type A, C, and G –Supplementary Fig.1–) for a $2 \times 2\sqrt{2} \times \sqrt{2}$ supercell containing 40 atoms. Quasi-harmonic free energies were calculated only for the lowest-energy configurations. Our spin-polarized DFT calculations were performed for bulk $BiFe_{0.5}Co_{0.5}O_3$ and $BiFe_{0.75}Co_{0.25}O_3$, hereafter referred to as $BFCO_{0.5}$ and $BFCO_{0.25}$.

Following a previous work by Diéguez and Íñiguez [38], we considered the four $BFCO_{0.5}$ crystal structures that are energetically most competitive at zero temperature. The crystal symmetry of such phases prior to introducing chemical disorder on the metal cation sites were tetragonal ($P4mm$), orthorhombic ($Pnma$), monoclinic (Pc), and rhombohedral ($R3c$). The optimized $BFCO_{0.5}$ structures resulting from such parent phases were labelled as $\mathcal{T}$, $\mathcal{O}$, $\mathcal{M}$, and $\mathcal{R}$, respectively (Supplementary Fig.1). Initially, a 20-atoms unit cell was employed to model all four polymorphs and to determine the atomic Co–Fe and magnetic spin arrangements (ferromagnetic –FM– and antiferromagnetic –AFM– of type A, C, and G –Supplementary Fig.1–) rendering the lowest energy for each phase (Fig.1). The $BFCO_{0.5}$ ground-state phase was identified as $\mathcal{T}$ with "C1" Co–Fe and AFM-C spin orderings (Fig.1) and an electric polarization of 140 μC/cm^2. The first metastable phase lies $\sim$ 45 meV/f.u. above the ground state and corresponds to a $\mathcal{R}$ structure presenting "C3" Co–Fe and AFM-G spin orderings (Fig.1) and an electric polarization of 45 μC/cm^2. It is worth noting that the energies of the $\mathcal{M}$ and $\mathcal{R}$ phases are practically degenerate in the AFM-G case. By using analogous computational methods to ours, Diéguez and Íñiguez [38] concluded that the $BFCO_{0.5}$ ground state was a $\mathcal{R}$ phase with AFM-G spin ordering. The reason for the discrepancy with our results lies on the fact that the DFT exchange-correlation functionals employed in both studies are different (Supplementary Fig.2). Nevertheless, our zero-temperature results appear to be more consistent with the recent observations by Azuma *et* al., in which the stable phase of $BFCO_{0.5}$ has been experimentally identified as $\mathcal{T}$ [27, 28].

To correctly describe the magnetic properties of the $\mathcal{T}$ and $\mathcal{R}$ phases at finite temperatures, we performed a systematic configurational analysis for a larger simulation cell containing 40 atoms (Fig.2). The $\mathcal{T}$ and $\mathcal{R}$ configurations were initialized with AFM-C and AFM-G spin orderings, respectively, thus rendering zero net magnetizations. Upon full optimization, however, a considerable fraction of states exhibited a net magnetization of either 0.5 or 0.25 μ_B/f.u. (Fig.2) due to spin imbalance between the Co and Fe sublattices (Supplementary Fig.3). The $\mathcal{T}$ phase with the lowest energy displayed AFM-C spin ordering and zero net magnetization, while the $\mathcal{R}$ ground state was ferrimagnetic (FiM) and presented a net magnetization of 0.50 μ_B/f.u. (Fig.2). At $T \neq 0$ conditions, each configuration contributes to the total magnetization according to the formula:

$$M(T) = \sum_{i}^{N_{\text{conf}}} M_i \cdot \frac{\exp\left(-\Delta E_i / k_B T\right)}{Z_{\text{conf}}} \ , \qquad (1)$$

where N_{conf} is the total number of configurations, M_i (E_i) the magnetization (energy) of the ith configuration, $\Delta E_i \equiv E_i - E_0$, E_0 the ground-state energy, k_B the Boltzmann constant, and $Z_{\text{conf}} \equiv \sum_i^{N_{\text{conf}}} \exp\left(-\Delta E_i / k_B T\right)$ the configurational partition function. By using Eq.(1) and the energy and configuration degeneracy data reported in Fig.2, we estimated that the net magnetization of the $\mathcal{T}$ and $\mathcal{R}$ phases amount both to 0.13 μ_B/f.u. near room temperature (Supplementary Fig.4). This result is consistent with a recent work by Gao *et* al. [29], in which robust ferrimagnetism has been experimentally demonstrated for $BFCO_{0.5}$ thin films at room temperature.

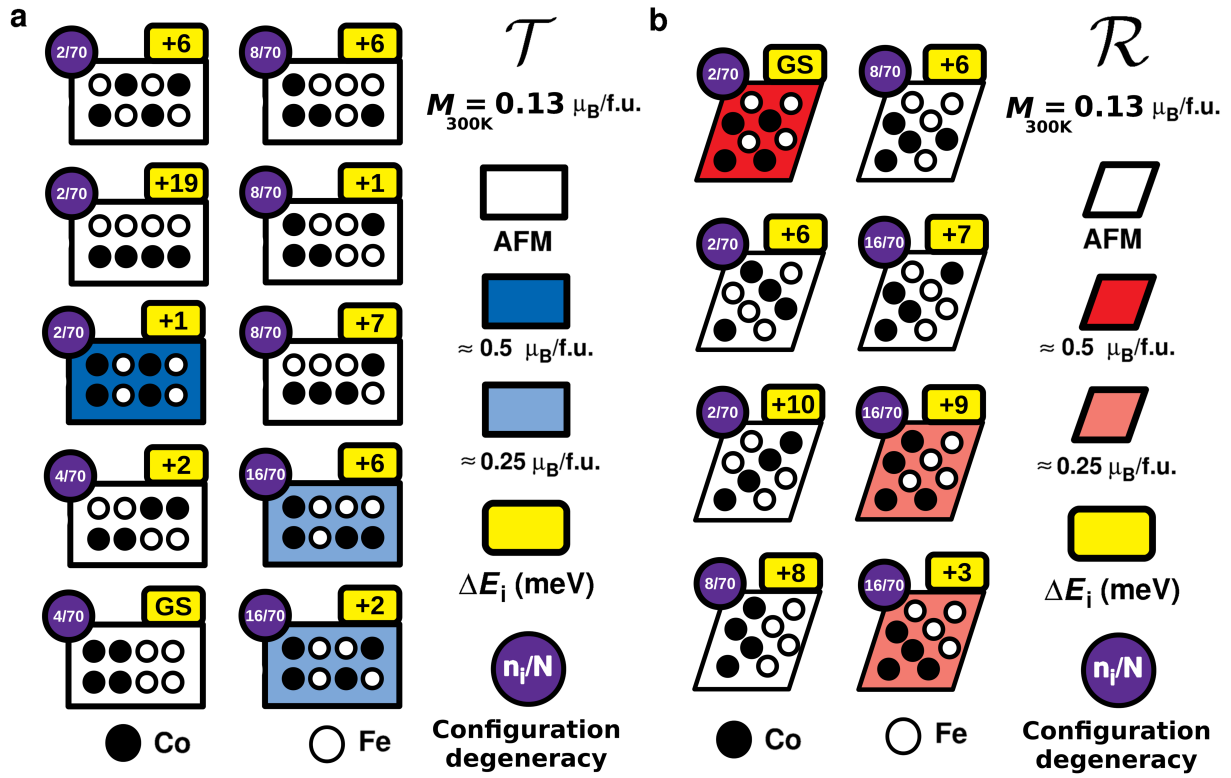

FIG. 2. First-principles determination of the magnetic properties of bulk $BFCO_{0.5}$ at finite temperatures for phases (**a**) $\mathcal{T}$ and (**b**) $\mathcal{R}$. All possible atomic Co–Fe arrangements were generated for a $2 \times 2\sqrt{2} \times \sqrt{2}$ simulation cell containing 40 atoms, which were reduced by crystal symmetry operations to 10 $\mathcal{T}$ and 8 $\mathcal{R}$ representative configurations [39]. The magnetic moment, total energy, and relative degeneracy of each representative configuration were calculated. The net magnetization estimated for each phase at room temperature is $\approx 0.13\ \mu_B$ per formula unit; "GS" stands for ground state and $\Delta E_i \equiv E_i - E_{\rm GS}$.

Figure 3a shows the P–T phase diagram estimated for bulk $BFCO_{0.5}$ with first-principles methods and the QH approximation [32, 35]. At low temperatures, a P-induced $\mathcal{T} \rightarrow \mathcal{R}$ phase transition occurs around 1 GPa that is characterized by a huge volume collapse of $\sim 10\%$ ($\Delta V = V_{\mathcal{T}} - V_{\mathcal{R}} > 0$), thus indicating a marked first-order behaviour. The corresponding P–T phase boundary, determined with the condition $\Delta G = G_{\mathcal{T}} - G_{\mathcal{R}} = 0$ where $G \equiv E + PV - TS$ represents the Gibbs free energy and S the entropy, presents a positive slope. Consequently, by the Clausius-Clapeyron relation $\Delta S/\Delta V = \partial P/\partial T$, the entropy of the $\mathcal{T}$ phase should be larger than that of the $\mathcal{R}$ phase, namely, $\Delta S = S_{\mathcal{T}} - S_{\mathcal{R}} > 0$. Our QH free-energy calculations explicitly confirm this result since the value of the Helmholtz free energy difference, $\Delta F = F_{\mathcal{T}} - F_{\mathcal{R}}$, decreases under uncreasing temperature (Fig.3d) and $\Delta S \equiv -\partial \Delta F/\partial T$. It is noted that the only type of entropy considered in our simulations is vibrational, hence the subscript "vib" in Fig.3d, since we assume that the magnetic and configurational contributions to S are small at low temperatures and very similar for the two phases (i.e., the $\{M_i\}$, $\{E_i\}$, and configurational degeneracy spectra calculated for $\mathcal{T}$ and $\mathcal{R}$ are much alike –Fig.2– [39]) hence they hardly have any influence on ΔG.

The $BFCO_{0.5}$ phase diagram shown in Fig.3a describes an unusual T-induced $\mathcal{R} \rightarrow \mathcal{T}$ phase transition occurring at room temperature and a moderate hydrostatic pressure of 1.2 ± 0.2 GPa, in which the electric polarization of the bulk material increases by $\sim 200\%$ (Supplementary Fig.4). Such a T-induced phase transformation involves two different ferroelectric FiM states and is mainly driven by the entropy contributions to their Gibbs free energy difference (that is, the ΔF term). This conclusion is deduced straightforwardly from Figs.3b-d, in which for a fixed P it is observed that the ΔE and $P\Delta V$ energy differences remain practically constant as a function of T (isovalue lines in Figs.3b,c are practically vertical), in marked contrast with ΔF (isovalue lines in Fig.3d are practically horizontal). It is worth noting that the T-induced $\mathcal{R} \rightarrow \mathcal{T}$ phase transition disclosed here for $BFCO_{0.5}$ has neither been predicted nor observed previously in bulk $BiCoO_3$ or $BiFeO_3$ thin films. For instance, the P–T phase boundary involving the super-tetragonal phase in bulk BCO presents a negative slope [18] due to the presence of stiff vibrational modes that reduce the vibrational entropy of the $\mathcal{T}$ phase as compared to that of other competing states [19, 20]. Consequently, by increasing temperature the stability of the $\mathcal{T}$ phase in bulk BCO is always reduced and the variation of the electric

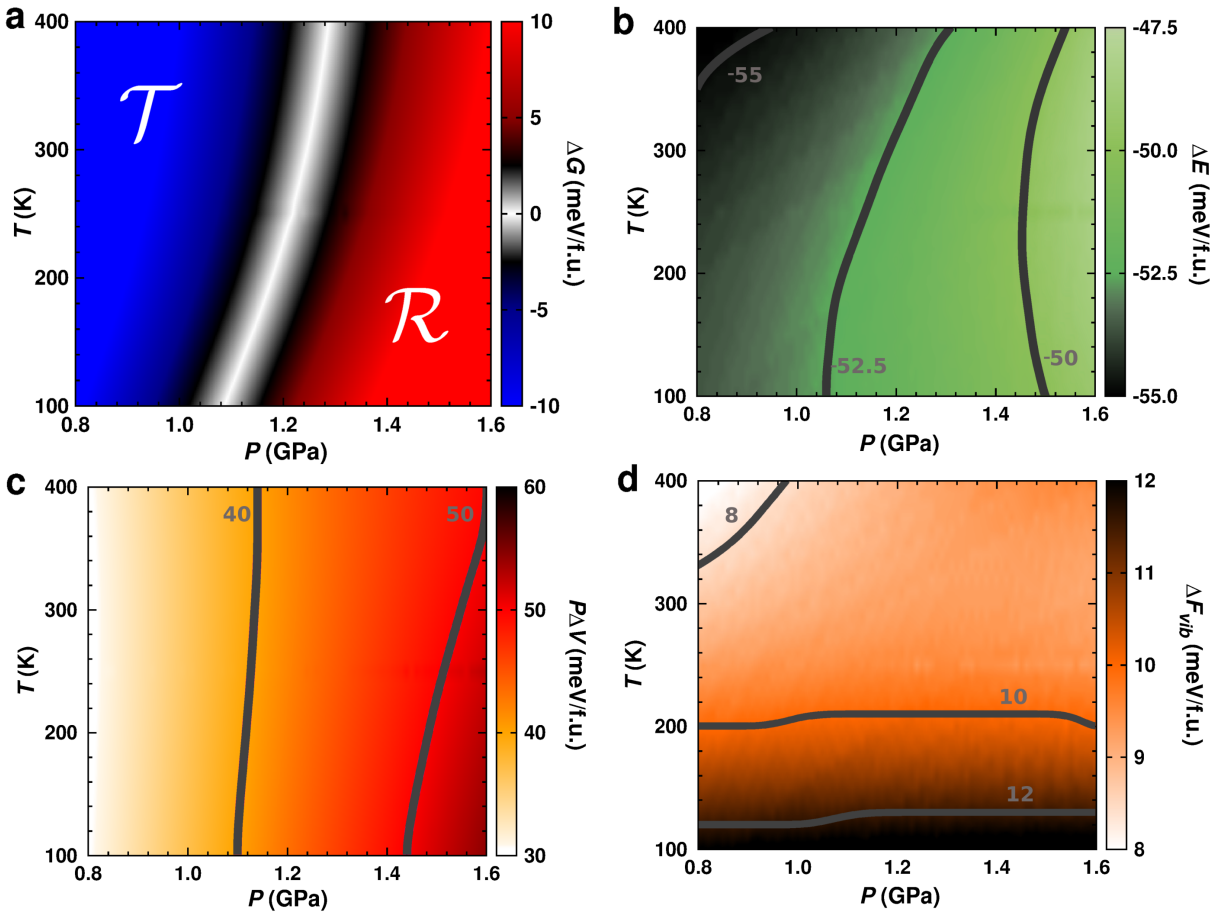

FIG. 3. Gibbs free energy difference between the $\mathcal{T}$ and $\mathcal{R}$ phases of bulk $BiFe_{0.5}Co_{0.5}O_3$ and their contributions expressed as a function of temperature and pressure ($\Delta A \equiv A_{\mathcal{T}} - A_{\mathcal{R}}$). **a** Total Gibbs free energy difference. **b** Static internal energy difference. **c** Enthalpy-related energy difference. **d** Vibrational Helmholtz free energy difference. Thermodynamic states presenting equal ΔA values are joined by thick solid lines.

polarization is negative ($dp/dT \ll 0$). A very similar behaviour has been found also for bulk $\mathcal{T}$ BFO [32].

In view of the prominent role played by the lattice excitations on the anomalous T-induced stabilization of the $\mathcal{T}$ phase at room temperature, we performed a detailed analysis on the phonon modes and frequencies of $BFCO_{0.5}$ (Fig.4). In particular, we estimated the projected density of vibrational states (PDOS) and Grüneisen parameter, defined as $\gamma_i \equiv -d\ln\omega_i/d\ln V$, for a large set of vibrational lattice frequencies, $\{\omega_i\}$ (the same than employed for the calculation of accurate QH free energies), for the $\mathcal{R}$ and $\mathcal{T}$ phases. The PDOS of $BFCO_{0.5}$ generally is characterized by a low-ω non-polar phonon region governed by Bi displacements ($0 < \omega \lesssim 4$ THz), followed by a medium-ω polar phonon interval dominated by transition-metal and oxygen ions ($4 \lesssim \omega \lesssim 10$ THz), and a high-ω non-polar phonon region governed almost exclusively by oxygen atoms ($\omega \gtrsim 10$ THz) (Fig.4 and Supplementary Fig.5). Since here we are interested in phase transitions occurring near room temperature, only those phonon excitations in the frequency interval $0 < \omega \lesssim 6$ THz are relevant (i.e., $k_B T_{\rm room} = 6.25$ THz and $\hbar\omega_i < k_B T_{\rm room}$ contribute the most to $F_{\rm vib}$ [40]). The number of Bi-dominated low-energy phonon modes is higher in the $\mathcal{R}$ phase than in the $\mathcal{T}$ phase (see PDOS peaks appearing at $\omega \approx 2$ THz in Fig.4), hence the positive sign of the ΔF energy difference (Fig.3d). However, the number of vibrational states with frequencies $2 \lesssim \omega \lesssim 6$ THz is larger in the $\mathcal{T}$ phase than in the $\mathcal{R}$ phase (e.g., "bell"-like lattice modes involving concerted transition metal and oxygen displacements are missing in the latter phase – Fig.4–) and consequently as the temperature is increased ΔF gets reduced, leading to $\Delta S > 0$. Meanwhile, positive (negative) γ values indicate vibrational phonon frequencies that become "stiffer" ("softer") under pressure since the bulk modulus of $BFCO_{0.5}$ is positive (as it occurs normally and we have explicitly checked). Consequently, based on the insets of Fig.4, upon compression the number of phonon frequencies in the interval $2 \lesssim \omega \lesssim 6$ THz is further depleted in the $\mathcal{R}$ phase as compared to that in the $\mathcal{T}$ phase (that is, $-10 \lesssim \gamma_{\mathcal{R}} \lesssim +50$ while $-2 \lesssim \gamma_{\mathcal{T}} \lesssim +1$). This last outcome explains the fact that the stability P span of the $\mathcal{T}$ phase becomes

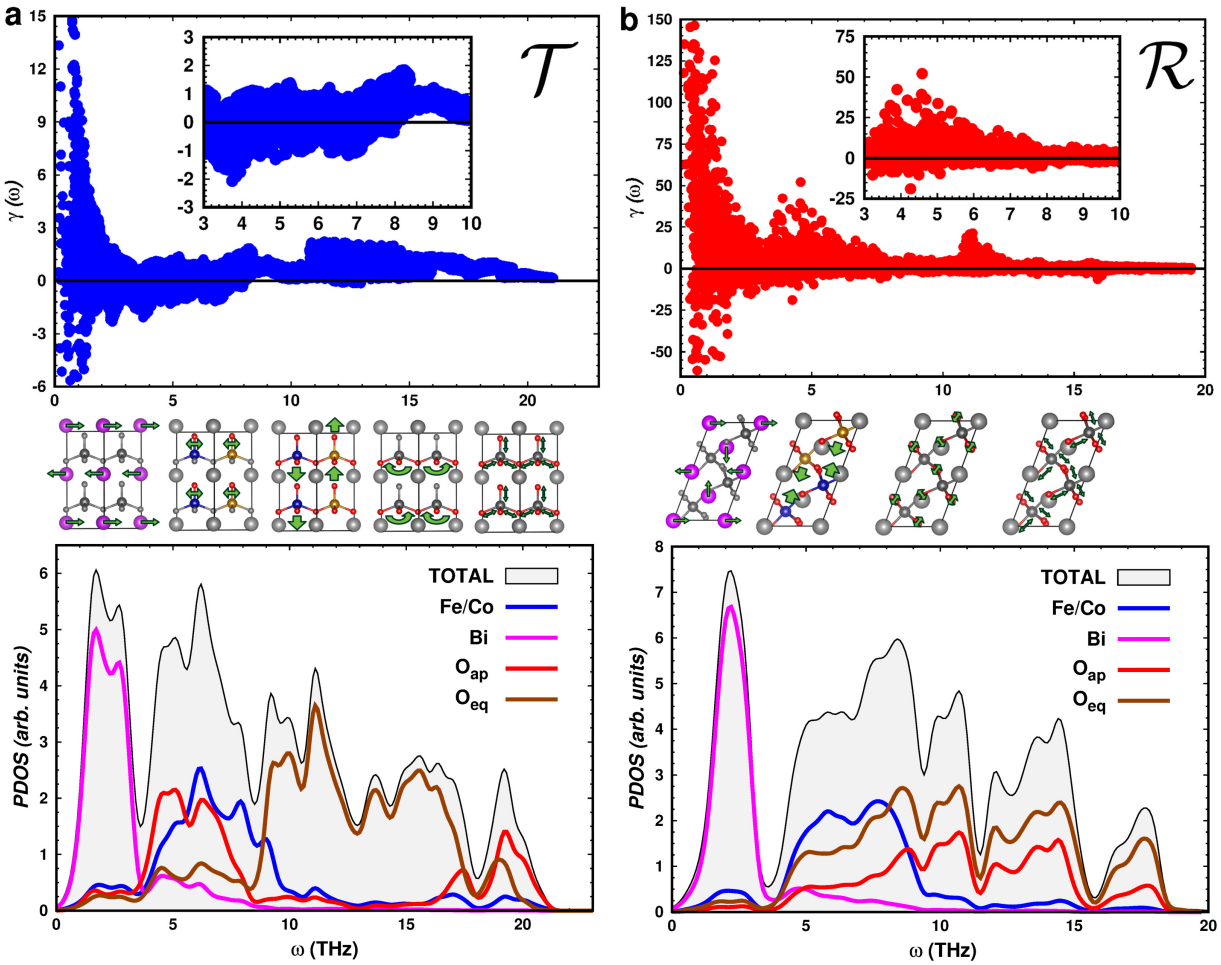

FIG. 4. Vibrational properties of the (**a**) $\mathcal{T}$ and (**b**) $\mathcal{R}$ phases of bulk $BiFe_{0.5}Co_{0.5}O_3$. The represented quantities are the Grüneisen parameter, $\gamma(\omega)$, and the density of vibrational states along with the corresponding ionic contributions (PDOS). O_{ap} and O_{eq} stand for oxygen atoms in apical and equatorial positions, respectively. Some representative phonon eigenmodes are sketched with green arrows and they are ordered according to their vibrational frequency.

wider as the temperature is increased, leading to the positive slope observed in the $\mathcal{T}$–$\mathcal{R}$ phase boundary (Fig.3a).

The unique entropically driven room-temperature stabilization of the $\mathcal{T}$ phase unravelled in this study for $BFCO_{0.5}$ occurs at a pressure of $\sim$ 1 GPa. For practical applications, it would be desirable that such a transformation was available at smaller compressions. Our DFT calculations carried out for $BFCO_{0.25}$ indicate that the critical pressure associated with the $\mathcal{T} \rightarrow \mathcal{R}$ phase transition, P_c, can be lowered drastically by means of composition. In particular, we estimate that P_c may be reduced by a staggering 70% by increasing the content of Fe in the solid solution from 50 up to 75% (Supplementary Fig.6). Interestingly, by repeating the same first-principles configurational analysis than performed for $BFCO_{0.5}$, we found that both the $\mathcal{R}$ and $\mathcal{T}$ phases of bulk $BFCO_{0.25}$ are also ferrimagnetic and exhibit a considerable net magnetization of 0.13 μ_B/f.u. near room temperature (Supplementary Figs.7–8). Moreover, the electric polarization of bulk $BFCO_{0.25}$ changes from 135 to 50 μC/cm^2 during the $\mathcal{T} \rightarrow \mathcal{R}$ phase transition (Supplementary Fig.8), which is very similar to the Δp shift estimated for $BFCO_{0.5}$. Therefore, we may conclude that the main characteristics of the transition involving the $\mathcal{R}$ and $\mathcal{T}$ phases in $BFCO_{0.5}$ at moderate pressures can be preserved and shifted down to practically ambient conditions by adjusting the relative content of Co–Fe cations in the solid solution. It is worth mentioning that the experimental BFCO phase diagram obtained by Azuma *et al.* as a function of temperature and composition appears to be consistent with our theoretical findings [27, 28]. In view of the low-cost and scalable chemical solution methods that are available for the synthesis of BFCO solid solutions [41], we expect that our theoretical work will stimulate new and exciting experimental research on $\mathcal{T}$ multiferroics.

In conclusion, we predict that a ferrimagnetic $\mathcal{T}$ phase can be stabilized under increasing T and P in bulk BFCO solid solutions near room temperature. This unusual T-induced phase transition involves a colossal increase in

the electric polarization of $\sim$ 200% and a volume expansion of $\sim$ 10%, which is of great potential for nanoelectronics and energy conversion applications. Polar phonon excitations involving mixed transition-metal and oxygen ion displacements play a decisive role on such an extraordinary phase transformation, which is neither observed nor predicted for any of the end members of the solid solution. Furthermore, the thermodynamic conditions at which the entropy-driven stabilization of the $\mathcal{T}$ phase occurs can be controlled adequately by varying the relative content of Co–Fe cations in the solid solution.

ACKNOWLEDGEMENTS

Computational resources and technical assistance were provided by the Australian Government and the Government of Western Australia through the National Computational Infrastructure (NCI) and Magnus under the National Computational Merit Allocation Scheme and The Pawsey Supercomputing Centre.

[1] L. Zhang *et al.*, Science **361**, 494 (2018).
[2] H. Yamada *et al.*, ACS Nano **7**, 5385 (2013).
[3] I. C. Infante *et al.*, Phys. Rev. Lett. **107**, 237601 (2011).
[4] X.-Y. Chen, L.-J. Chen, X.-B. Yang, Y.-J. Zhao, H.-C. Ding, and C.-G. Duan, J. Appl. Phys. **111**, 013901 (2012).
[5] C.-Y. Kuo *et al.*, Nat. Commun. **7**, 12712 (2016).
[6] J.-G. Park, M. D. Le, J. Jeong, and S. Lee, J. Phys. Condens. Matter **26**, 433202 (2014).
[7] J. T. Heron *et al.*, Nature **516**, 370 (2014).
[8] J. Allibe *et al.*, Nano Lett. **12**, 1141 (2012).
[9] J. P. Domann and G. P. Carman, J. Appl. Phys. **121**, 044905 (2017).
[10] T. Nan *et al.*, Nat. Commun. **8**, 296 (2017).
[11] H. Yamamoto, T. Ogata, Y. Saki, and M. Azuma, Inorg. Chem. **58**, 2755 (2019).
[12] Z. Pan *et al.*, Chem. Mater. **31**, 1296 (2019).
[13] Ll. Mañosa and A. Planes, Adv. Mater. **29**, 1603607 (2017).
[14] C. Cazorla, Appl. Phys. Rev. **6**, 041316 (2019).
[15] J. Min, A. K. Sagotra, and C. Cazorla, Phys. Rev. Mater. **4**, 015403 (2020).
[16] A. A. Belik *et al.*, Chem. Mater. **18**, 798 (2006).
[17] J. Wang *et al.*, Science **299**, 1719 (2003).
[18] K. Oka *et al.*, J. Am. Chem. Soc. **132**, 9438 (2010).
[19] C. Cazorla, O. Diéguez, and J. Íñiguez, Sci. Adv. **3**, e1700288 (2017).
[20] C. Cazorla and J. Íñiguez, Phys. Rev. B **98**, 174105 (2018).
[21] Y. Heo *et al.*, ACS Nano **11**, 2805 (2017).
[22] J. Wojdel and J. Íñiguez, Phys. Rev. Lett. **105**, 037208 (2010).
[23] G. J. MacDougall *et al.*, Phys. Rev. B **85**, 100406(R) (2012).
[24] C. R. Bowen, J. Taylor, E. LeBoulbar, D. Zabek, A. Chauhan, and R. Vaish, Energy Environ. Sci. **7**, 3836 (2014).
[25] M. Hoffmann, U. Schroeder, C. Künneth, A. Kersch, S. Starschich, U. Böttger, and T. Mikolajick, Nano Energy **18**, 154 (2015).
[26] T. Gottschall *et al.*, Nat. Mater. **17**, 929 (2018).
[27] M. Azuma, S. Niitaka, N. Hayashi, K. Oka, M. Takano, H. Funakubo, and Y. Shimakawa, Jpn. J. Appl. Phys. **47**, 7579 (2008).
[28] H. Hojo, K. Oka, K. Shimizu, H. Yamamoto, R. Kawabe, and M. Azuma, Adv. Mater. **30**, 1705665 (2018).
[29] B. Gao *et al.*, Phys. Rev. Mater. **2**, 084401 (2018).
[30] G. Kresse and J. Furthmüller, Phys. Rev. B **54**, 11169 (1996).
[31] J. P. Perdew, K. Burke, and M. Ernzerhof, Phys. Rev. Lett. **77**, 3865 (1996).
[32] C. Cazorla and J. Íñiguez, Phys. Rev. B **88**, 214430 (2013).
[33] P. E. Blöchl, Phys. Rev. B **50**, 17953 (1994).
[34] C. Cazorla and M. Stengel, Phys. Rev. B **92**, 214108 (2015).
[35] C. Cazorla and J. Boronat, Rev. Mod. Phys. **89**, 035003 (2017).
[36] G. Kresse, J. Furthmüller, and J. Hafner, Europhys. Lett. **32**, 729 (1995).
[37] D. Alfè, Comp. Phys. Commun. **180**, 2622 (2009).
[38] O. Diéguez and J. Íñiguez, Phys. Rev. Lett. **107**, 057601 (2011).
[39] J. N. Shenoy, J. N. Hart, R. Grau-Crespo, N. L. Allan, and C. Cazorla, Adv. Theory Simul. **2**, 1800146 (2019).
[40] C. Cazorla and T. Gould, Sci. Adv. **5**, eaau5832 (2019).
[41] P. Machado *et al.*, Chem. Mater. **31**, 947 (2019).